Chemical Engineering Journal 109 (2005) 37–47

Chemical Engineering Journal

www.elsevier.com/locate/cej

Local bubble size distributions, gas–liquid interfacial areas and gas holdups in a stirred vessel with particle image velocimetry

Marko Laakkonen [a,*], Markus Honkanen [b], Pentti Saarenrinne [b], Juhani Aittamaa [a]

[a] *Helsinki University of Technology, Laboratory of Chemical Engineering, P.O. Box 6100, FIN-02015 HUT, Espoo, Finland*
[b] *Tampere University of Technology, Laboratory of Energy and Process Engineering, P.O. Box 589, FIN-33101, Tampere, Finland*

Received 14 April 2004; received in revised form 1 March 2005; accepted 1 March 2005

Abstract

Particle image velocimetry (PIV) was used to measure local bubble size distributions (BSD), gas–liquid interfacial areas, gas holdups and flow velocities simultaneously from a flat-blade turbine agitated 14 dm^3 vessel. Air–water and CO_2–*n*-butanol systems were investigated at several agitation conditions in order to find out the effect of physical properties on the vessel hydrodynamics. Dispersion was illuminated with a laser light sheet to minimise the blurriness in the images. The depth of field (DOF), needed in the calculation of local gas–liquid interfacial areas and gas holdups was obtained from the calibration experiments with a bubble gel. A simple method was developed to correct some bias errors of the measurement technique. Calibration experiments verified the need and the relevance of the developed correction. The measured BSDs varied reasonably with the measurement point in both air–water and CO_2–*n*-butanol systems and were in agreement with the well-known correlations of Calderbank [P.H. Calderbank, Physical rate processes in industrial fermentation. Part 1. The interfacial area in gas–liquid contacting with mechanical agitation, Trans. Inst. Chem. Engrs. 36 (1958) 443–463]. The results show that local hydrodynamic quantities can be measured simultaneously with the PIV from a stirred vessel. This is a benefit, since more consistent experimental information is obtained for the validation of gas–liquid stirred tank simulation tools.

Keywords: Agitation; Bubble size distribution; Interfacial area; Gas holdup; Particle image velocimetry

1. Introduction

Agitated gas–liquid vessels are widely used as reactors in chemical, biochemical, petroleum and mining industries. Gas–liquid mass transfer is a common rate-determining step in agitated reactors. Local mass transfer areas depend on the bubble sizes and concentrations and vary notably even in small stirred tanks [1–4]. This motivates the use of bubble size distributions (BSD) rather than averaged bubble sizes in the reactor simulation tools. Population balance is a fundamental approach for the modelling of local BSDs. Computational fluid dynamic (CFD) tools along with population balance models give insight into local vessel conditions and are therefore useful for the design and scale-up of industrial agitated reactors, in which mass transfer conditions vary, often notably. Gas–liquid CFD models are still uncertain and need validation against local experimental information [5].

The measurement of turbulent gas–liquid dispersions is challenging and many experimental techniques are available [6–9]. Optical imaging techniques have been used commonly to investigate bubble sizes in stirred tanks [9–14]. Takahashi and Nienow [11] used a photographing technique for the measurement of local gas holdups from a lean agitated dispersion. Particle image velocimetry (PIV) is a versatile optical technique, which can be used to investigate flow fields and turbulence quantities in gas–liquid systems [15–18].

The aim of the present work was to investigate several interesting properties of gas–liquid flow simultaneously in order to produce more consistent experimental information for the validation of simulation tools for agitated gas–liquid reactors. Local BSDs, gas–liquid interfacial areas and gas holdups were measured from air–water and CO_2–*n*-butanol

* Corresponding author. Tel.: +358 9 4512642; fax: +358 9 4512694.
E-mail address: marko.laakkonen@hut.fi (M. Laakkonen).

1385-8947/$ – see front matter © 2005 Elsevier B.V. All rights reserved.
doi:10.1016/j.cej.2005.03.002

systems in a laboratory stirred tank with a PIV apparatus. A simple method was developed to correct bias errors of the measurement technique. Flow fields and turbulence quantities were investigated simultaneously and have been reported by Honkanen and Saarenrinne [18].

2. The processing of PIV results

Digital cameras and automatic image analysis have made quantitative optical measurements easier. A statistically representative sample of bubbles can be identified from the images by using bubble identification algorithms, although this is not an easy task especially from dense dispersions. The overlapping of bubbles in the images, the blurriness of bubbles that are out of focus and the distortions in bubble shape make the automatic identification of bubbles demanding [19]. Honkanen and Saarenrinne [20] have proposed a robust object detection method employed with algorithms that detect and separate the overlapping objects and study the objects individually. This method can be applied to denser dispersions where identification is difficult due to overlapping of bubbles in the images.

The success of bubble identification depends on the quality of image and the lighting conditions. Large number of bubbles between the camera and the investigated position weakens the image quality. A careful arrangement of camera and light sources is needed to avoid the overexposure of bubbles and the optical distortions from the vessel walls. Backlighting, where the light source and camera are opposite each other has been used most commonly [19]. Although the bubble sizes and shapes are identified well and the overexposure of bubbles is minimised, the use of backlighting is not possible at high bubble concentrations and large dispersion volumes due to blurriness in the images. The background noise can be minimised by illuminating the dispersion with a laser light sheet, which is perpendicular to the camera. Bubble concentrations, local gas–liquid interfacial areas and gas holdups can be calculated from these experiments, if the effective depth of field is known.

2.1. Measurement volume

Calibration experiments with a bubble gel showed that the use of laser light sheet for the illumination of bubbles and the automated identification of bubbles with a thresholding algorithm cause the underestimation of bubble size [18]. An explanation is that some bubbles have less than 50% of their volume inside the light sheet. This has been illustrated in Fig. 1. In addition, large bubbles are observed from a larger volume of dispersion than small bubbles [19]. The height H_P and the width W_P of picture are known accurately, but the effective depth of field (DOF) depends on the bubble size and the depth of laser light sheet. As can be concluded from Fig. 1, the volume of dispersion $V(d_j)$ from which a bubble

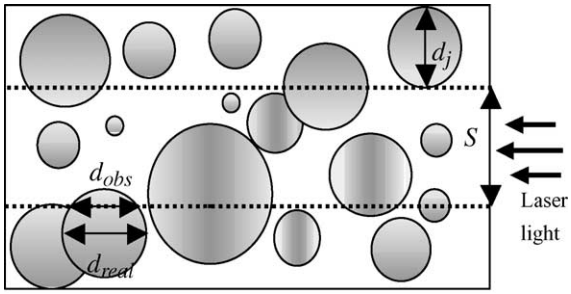

Fig. 1. Possible locations of bubbles in a cross-section of laser light sheet. The depth of laser light sheet s, the observed d_{obs} and the actual d_{real} bubble size.

of size d_j is observed in an experiment is

$$V(d_j) = N_P W_P H_P (s + 2d_j), \tag{1}$$

where N_P is the number of recorded pictures in an experiment.

2.2. Number, area and volume densities of bubbles

Number, area and volume density distributions of bubbles are obtained by classifying the measured bubbles into finite sized categories. Letting index i denote a size category and index $j = 1, \ldots, \mathrm{NBC}$ an individual measured bubble belonging to category i, number, area and volume densities for each size category i are obtained from

$$n(d_i) = \frac{1}{\Delta d_i} \sum_{j=1}^{\mathrm{NBC}} \frac{1}{V(d_j)}, \tag{2}$$

$$a(d_i) = \frac{1}{\Delta d_i} \sum_{j=1}^{\mathrm{NBC}} \frac{a_{b,j}}{V(d_j)}, \tag{3}$$

$$v(d_i) = \frac{1}{\Delta d_i} \sum_{j=1}^{\mathrm{NBC}} \frac{v_{b,j}}{V(d_j)}, \tag{4}$$

The bubble number, area and volume concentrations are obtained by integrating the density functions (2)–(4) over the discretization size range.

$$n_t = \sum_{i=1}^{\mathrm{NC}} n(d_i) \Delta d_i \tag{5}$$

$$a_t = \sum_{i=1}^{\mathrm{NC}} a(d_i) \Delta d_i \tag{6}$$

$$v_t = \sum_{i=1}^{\mathrm{NC}} v(d_i) \Delta d_i \tag{7}$$

2.3. A statistical correction

A correction, similar to what Rohani and Tadayyon [21] proposed for the Par-Tec® 100 analyzer, is derived to correct

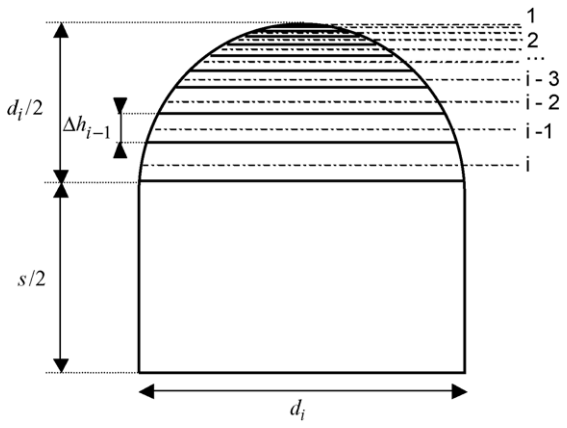

Fig. 2. A geometrical visualisation of statistical correction.

the biased BSDs. For the symmetry reasons it is sufficient to consider only one half of the laser light sheet in the derivation. It is assumed that bubbles are spherical and their actual diameter is observed only, when more than 50% of the bubble volume is inside the laser light sheet. The observed size of a bubble depends on its position in the light sheet (Fig. 1). When the bubble of size d_i crosses the light sheet, the probability to observe it as a smaller one in a size category $j = 1, \ldots, i-1$ is obtained from the following expression based on geometry in Fig. 2:

$$p(d_j, d_i) = \frac{\Delta h_j}{s/2 + d_i/2}. \tag{8}$$

The height of bubble size category Δh_j is calculated from Eq. (9) based on trigonometry and Fig. 2:

$$\Delta h_j = \sqrt{\left(\frac{d_i}{2}\right)^2 - \left(\frac{2d_j - \Delta d_j}{4}\right)^2} - \sqrt{\left(\frac{d_i}{2}\right)^2 - \left(\frac{2d_j + \Delta d_j}{4}\right)^2}, \tag{9}$$

where d_j is the characteristic size and Δd_j the width of bubble size category j. The measured $n_M(d_j)$ and the actual (corrected) $n_C(d)$ number densities can now be related through

$$n_M(d_j) = \sum_{i=j}^{NC} (C_n(d_j, d_i) p(d_j, d_i) n_C(d_i)), \tag{10}$$

where NC is the number of discretization categories and $C_n(d_j,d_i)$ is the scaling parameter needed to transform the bubble number density from category i to j. The number density depends on the width of category Δd_j and the volume of dispersion $V(d_i)$, which causes the need of the following scaling factor:

$$C_n(d_j, d_i) = \left(\frac{V(d_i)}{V(d_j)}\right)\left(\frac{\Delta d_i}{\Delta d_j}\right). \tag{11}$$

The corrected area $a_C(d_i)$ and $v_C(d_i)$ volume densities are obtained similarly by replacing the $n_M(d_j)$, $n_C(d_i)$ and $C_n(d_j,d_i)$ with the corresponding quantities in Eq. (10). To transform the bubble area density from one size category to another requires the scaling of dispersion volume, bubble surface area and width of category

$$C_a(d_j, d_i) = \left(\frac{V(d_i)}{V(d_j)}\right)\left(\frac{d_j^2}{d_i^2}\right)\left(\frac{\Delta d_i}{\Delta d_j}\right). \tag{12}$$

Respectively, the dispersion and bubble volume and the width of size category need to be scaled, when bubble volume density is transformed from category i to j

$$C_v(d_j, d_i) = \left(\frac{V(d_i)}{V(d_j)}\right)\left(\frac{d_j^3}{d_i^3}\right)\left(\frac{\Delta d_i}{\Delta d_j}\right). \tag{13}$$

From algebraic equations (10) we end up to the matrix equation, which includes NC bubble size categories.

$$\begin{bmatrix} n_M(1) \\ n_M(2) \\ \vdots \\ n_M(NC) \end{bmatrix} = \begin{bmatrix} p(1,1)C_n(1,1) & \cdots & \cdots & p(1,NC)C_n(1,NC) \\ 0 & p(2,2)C_n(2,2) & \cdots & p(2,NC)C_n(2,NC) \\ 0 & 0 & \cdots & \cdots \\ 0 & 0 & 0 & p(NC,NC)C_n(NC,NC) \end{bmatrix} \times \begin{bmatrix} n_C(1) \\ n_C(2) \\ \vdots \\ n_C(NC) \end{bmatrix} \tag{14}$$

The corrected number density BSDs n_C are obtained by solving the matrix equation (14). The corrected area and volume density BSDs are solved from corresponding matrix equations. Local bubble concentrations, gas–liquid interfacial areas and gas volume fractions are obtained from Eqs. (5)–(7).

3. Experimental

3.1. Experimental setup

Experiments were made in a 14 dm^3 flat-bottomed, cylindrical glass vessel. The vessel was agitated by a flat-blade impeller and was fully baffled. The vessel was placed into a rectangular container to minimise the optical reflections from its rounded wall. Gas was distributed through a 0.66 mm tube nozzle to the bottom of vessel below the impeller. PIV apparatus consisted of two CCD cameras and Nd-YAG-laser (400 mJ) that were mounted to the optical bench. Experimental positions (A–F) and dimensions of stirred vessel are presented in Fig. 3.

Local BSDs were measured from air–tap water and CO_2–*n*-butanol systems at several agitation conditions in or-

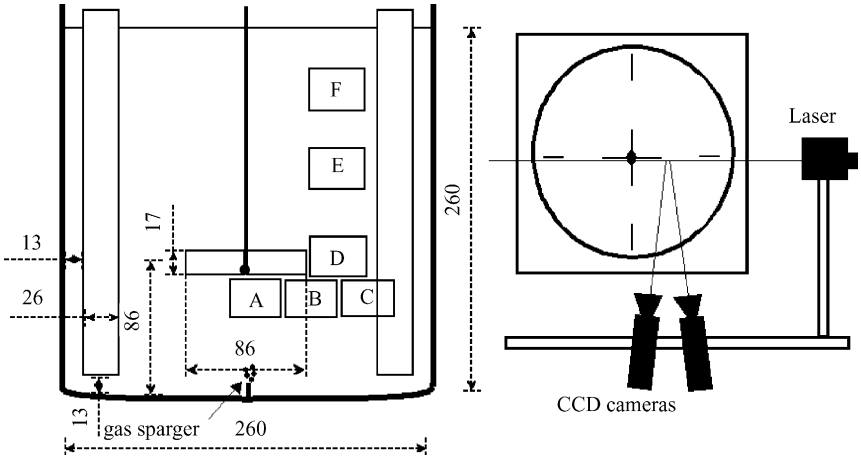

Fig. 3. Dimensions of stirred vessel (left) in millimeters and a top view of the experimental setup (right).

der to find the effect of physical properties on vessel hydrodynamics. Low gassing rates (0.013–0.072 vvm) were used to get a disturbance-free optical access to the investigated positions inside the dispersion (Fig. 3). Stirring speeds 400 and 500 rpm were selected so that gas was well dispersed and the surface aeration was minimal. Experiments were made at laboratory temperature 22 °C and atmospheric pressure. The measured surface tensions were for the tap water 69.5 mN/m and *n*-butanol 23.2 mN/m.

Approximately 500 pictures, including 4000–70 000 bubbles were recorded in each experiment. The imaged areas were from 16.6 mm × 24.3 mm to 30.5 mm × 40 mm producing the smallest detectable bubble size of about 0.1 mm. The dispersion was illuminated with a laser light sheet to minimise the blurriness in the images. The bubbles, which touched the laser light sheet were observed in the PIV images. The aperture of camera was adjusted to the smallest possible value (f-number 11) to avoid the overexposure of bubbles. The f-number 11 yielded the depth of field 8 mm. Glass spheres of size 10 μm were used as tracer particles to enable the measurement of turbulence quantities, bubble and liquid velocities simultaneously [18].

3.2. Depth of laser light sheet

The intensity profile of laser beam is close to a Gaussian curve and becomes flatter when its depth increases. Deep light sheet makes the overexposure of bubbles less probable and improves the measurement accuracy of gas holdup. The depth of light sheet controls the DOF and is needed to calculate local bubble concentrations, gas–liquid interfacial areas and gas volume fractions.

The depth of light sheet was determined from the calibration experiments with a bubble gel. The imaging experiments were made by varying the location of laser light sheet relative to the stagnant bubbles in the gel. The calibration would have been impossible with air bubbles in water or CO_2 bubbles in *n*-butanol, since the rising bubbles fluctuate and their position is not known accurately. Although a small bias is possible, the depth of laser light sheet obtained from the experiments with the bubble gel should apply relatively well for the air–water and CO_2–*n*-butanol systems.

The effective depth of field (DOF) was 11 mm for the 2.0 mm bubble inside the gel. In the middle of light sheet 2.0 mm bubble was detected correctly at the depth of 5 mm while at the edge of light sheet the measured size varied between 1.1 and 1.8 mm. In the second calibration experiment, the DOF was 8 mm for the 0.75 mm bubble. The resulting depth of laser light sheet is from the first calibration experiment 11.0 mm − 2 × 2.0 mm = 7.0 mm and from the second calibration experiment 8.0 mm − 2 × 0.75 mm = 6.5 mm.

3.3. Identification of bubbles

A threshold method was used to identify bubbles from the PIV images. It identifies pixel segments, which have a sufficiently strong light intensity and a sufficiently large pixel area [18], and gives a high contrast between the bubble outline and the background. Bubbles were detected from the identified pixel segments as ellipsoids. Imaginary spherical bubbles of equivalent volume were calculated assuming bubbles to oblate ellipsoids. The characteristic diameter of an imaginary spherical bubble is

$$d = (d_{\text{long}}^2 d_{\text{short}})^{1/3}, \tag{15}$$

where d_{short} and d_{long} are the minor and major axes of ellipsoid in the PIV image. Finally, the procedure presented in Section 2 was applied to correct the bias errors and calculate local gas–liquid interfacial areas and gas holdups.

4. Results and discussion

4.1. Accuracy of bubble detection

The bubble identification algorithm failed occasionally with the overexposed or blurred bubbles. Sometimes a group of bubbles was observed as a single bubble or one large bubble was detected as a group of several small bubbles. These errors should, however, compensate each other to some extend. At higher bubble concentrations the bubbles in front of light sheet hampered the visibility resulting blurriness in the bubble images. Due to overlapping of bubbles the identification was most demanding from the images in experimental positions A and B, where gas volume fractions were larger than elsewhere.

4.2. Relevance of statistical correction

Measured bubbles were distributed to 20 size categories. This produced smooth BSDs without hiding the shape of BSD. The calibration experiments verified the assumptions made in the derivation of correction, namely, that bubbles are observed as smaller than their actual size at the edge of the laser light sheet. The 6.5 mm depth of the laser light sheet obtained from the calibration experiment with a 0.75 mm bubble in the gel was used to process the measured BSDs. The sensitivity of calculated results to the depth of laser light sheet was checked by varying the depth in the range 5–8 mm. Test calculations revealed a 15% relative change of gas holdup at maximum.

The correction of bias errors was applied for the characteristic diameters of imaginary spherical bubbles, despite the fact that bubbles were identified from the PIV images as oblate ellipsoids. The correction could probably be developed for the ellipsoidal bubbles as well, although it would become more complicated. It must, however, be noted that bubbles were mainly smaller than 4 mm and deviated only slightly from the spherical, which justifies the assumption of spherical bubbles in the correction.

The dependence of DOF on the bubble size had a significant effect on the volume density distributions. This is illustrated in Fig. 4, where a measured volumetric BSD calculated assuming a constant DOF is presented with markers. The solid line represents the corresponding corrected BSD where the underestimation of bubble size and the dependence of DOF on the bubble size are considered. The correction decreases bubble volume densities, since large bubbles have larger DOF than small bubbles. The effect of correction is best illustrated by the gas–liquid interfacial area and the gas holdup. Without the correction interfacial area is 29 m^2/m^3 and holdup 0.74 vol.% for the experiment presented in Fig. 4. The corresponding corrected values 21 m^2/m^3 and 0.48 vol.% are notably smaller, which shows the relevance of correction.

The correction shifts volume density peak towards larger bubble size. The effect of correction on the shape of BSD is small, since relatively deep laser light sheet was used to avoid

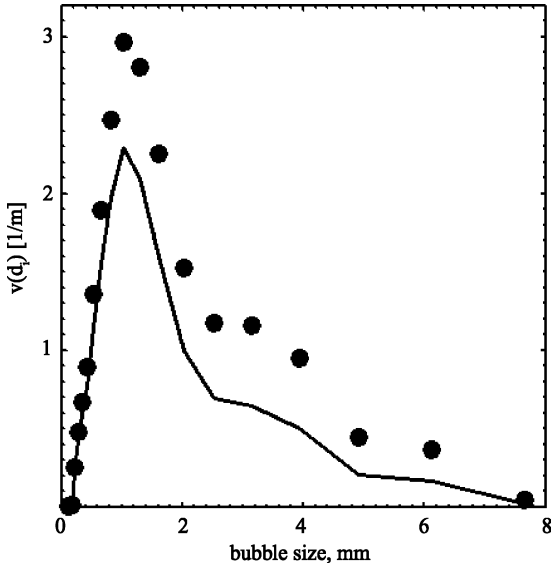

Fig. 4. Bubble volume density distribution: (●) uncorrected and (—) corrected, air–water system, experimental position D, $N = 500$ rpm, $Q = 0.072$ vvm.

the overexposure of bubbles. On the other hand, a deep light sheet favours the overlapping of bubbles in the images. For instance, Takahashi and Nienow [11] measured local bubble sizes and gas holdups by a photographing technique by using a focal depth of about 50 mm. Dispersions were extremely lean in their experiments in order to produce high quality photographs and probably also to avoid the overlapping of bubbles in the images. It is emphasized that the correction becomes significant especially with a narrow laser light sheet. A narrow sheet avoids the overlapping of bubbles in the images and allows more accurate planar velocity measurements as the flow field becomes less three-dimensional.

4.3. Local bubble size distributions

Available models for predicting bubble sizes are mostly semi-empirical correlations where vessel-averaged mean bubble sizes are related to the balance between interfacial tension and turbulent stresses based on the Kolmogoroff's theory [1,22]. This approach has been criticised by postulating that coalescence rather than breakage controls the bubble size. Marucci [23] proposed that coalescence depends on the drainage time of liquid film between the colliding bubbles and coalescence can be inhibited by the surfactants that immobilise the bubble surface. The interfacial phenomena depend on the concentrations of solutes and the interfacial concentration gradients, but they are not easily related to the interfacial tension. Machon et al. [12] measured bubble sizes with photography from electrolyte and alcohol solutions and concluded that there is no correlation between the bubble size and the surface tension. Although surfactants are present in many industrial applications, coalescence is often significant and needs to be considered in the modelling of gas–liquid flows. Therefore, local BSDs must be

investigated in coalescing systems as was done in the present work.

The well-known correlation of Calderbank [1] gives mean bubble size in a stirred tank

$$d_{32} = 4.15\left[\frac{\sigma^{0.6}}{(P_g/V)^{0.4}\rho_C^{0.2}}\right]v_t^{0.5} + 0.0009. \quad (16)$$

It is based on the local gas–liquid area and gas holdup experiments with ten liquids in baffled 5 and 100 dm^3 vessels agitated by Rushton turbine. Similarly as in this work, the investigated liquids included water and *n*-butanol. Interfacial areas were measured by a light-scattering method and local gas holdups by sampling dispersion to an evacuated glass bulb. The following correlation was developed for the vessel-averaged gas holdup [1]:

$$v_t = \left(\frac{U_s v_t}{U_t}\right)^{0.5} + 0.000216 \times \left[\frac{(P_g/V)^{0.4}\rho_C^{0.2}}{\sigma^{0.6}}\right]\left(\frac{U_s}{U_t}\right)^{0.5}, \quad (17)$$

where U_s is the superficial gas velocity and U_t the bubble terminal velocity, which is 0.265 m/s [1]. Although the bubble rise velocities actually depends on the bubble size, $U_T = 0.265$ m/s should be used in (17), because Calderbank [1] used this value in the fitting of his correlation. In the absence of agitation (17) reduces to $v_t = U_s/U_t$. The correlations (16) and (17) were developed based on the experiments with Rushton turbines, but they should be applicable for the flat-blade impeller agitated vessel as well. This assumption is justified by the observations of Alves et al. [24] who compared available experimental studies and made a conclusion that differences in bubble sizes cannot be attributed to the size of tank, number or type of impellers or measuring method. The vessel-averaged Sauter mean bubble sizes predicted by Eq. (16) and the measured local mean bubble sizes are compared in Fig. 5a and b. The impeller power number 3.4 needed to calculate the power requirement of mixing was obtained from the correlation of Sano and Usui [25]. Testing of available literature correlations showed that due to low gassing rates the correction of mixing power due to gassing was not necessary. The gas holdups needed by (16) were calculated from Eq. (17). The measured gas holdups were used to calculate experimental points in Fig. 5a and b.

Fig. 5a shows good agreement between correlation (16) and experiments for the air–water system. In the CO_2–*n*-butanol system (Fig. 5b), measured local bubble sizes are larger than the predicted. As can be concluded from Fig. 5a and b, bubble size varies notably in the vessel in both systems making the comparison difficult. Assuming that the measured positions A–F represent the inhomogeneities of bubble sizes in the vessel, the vessel-averaged Sauter mean bubble size is obtained as an arithmetic average from the local bubble sizes. At stirring speed 400 rpm and gassing rate 0.037 vvm the vessel-averaged mean bubble size is for the air–water system 2.0 mm and for the CO_2–*n*-butanol system 2.3 mm. The values predicted by the correlation (16) are 1.9 and 1.6 mm, respectively. It is possible that due to higher gas holdups the overlapping of bubbles occurred more frequently in the images from CO_2–*n*-butanol than air–water system. A group of small overlapping bubbles was identified occasionally as a single large bubble. This could explain the larger bubbles compared to the air–water experiments and the correlation (16).

The gas injection below the impeller explains the large bubbles in the measurement positions A and B. Bubbles are smallest close to the liquid surface in positions E and F, although some coalescence should occur as bubbles go far from the impeller. Also Schäfer et al. [26] observed larger bubbles in the impeller discharge flow compared to the regions far from impeller in the mixture of silicone oils. They suggested that large primary bubbles rising from the gas distributor or trailing gas vortices in the impeller discharge flow explain the large bubbles in the impeller region compared to other vessel regions.

Some local volumetric BSDs are presented in Fig. 6a–d. The heights of bubble volume density distributions are scaled to unity to highlight their shape. The BSDs are asymmetrical

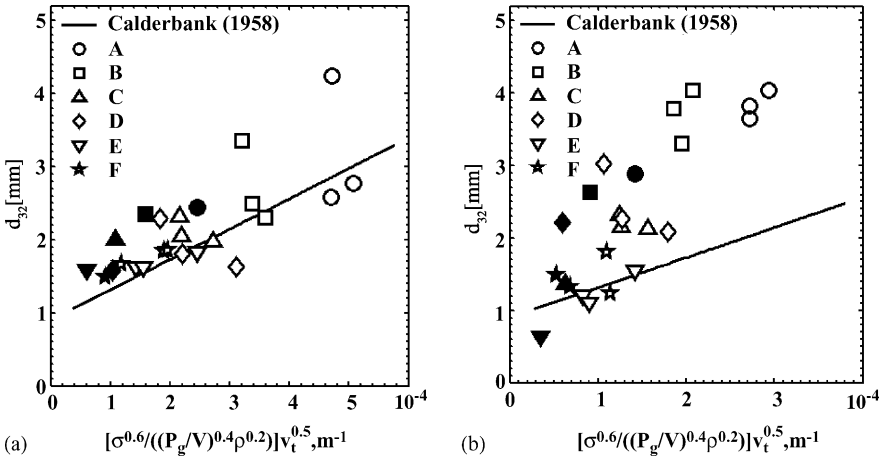

Fig. 5. Measured local (A–F) and predicted [1] Sauter mean bubble sizes: (a) air–water, (b) CO_2–*n*-butanol system, open markers $N = 400$ rpm, filled markers $N = 500$ rpm.

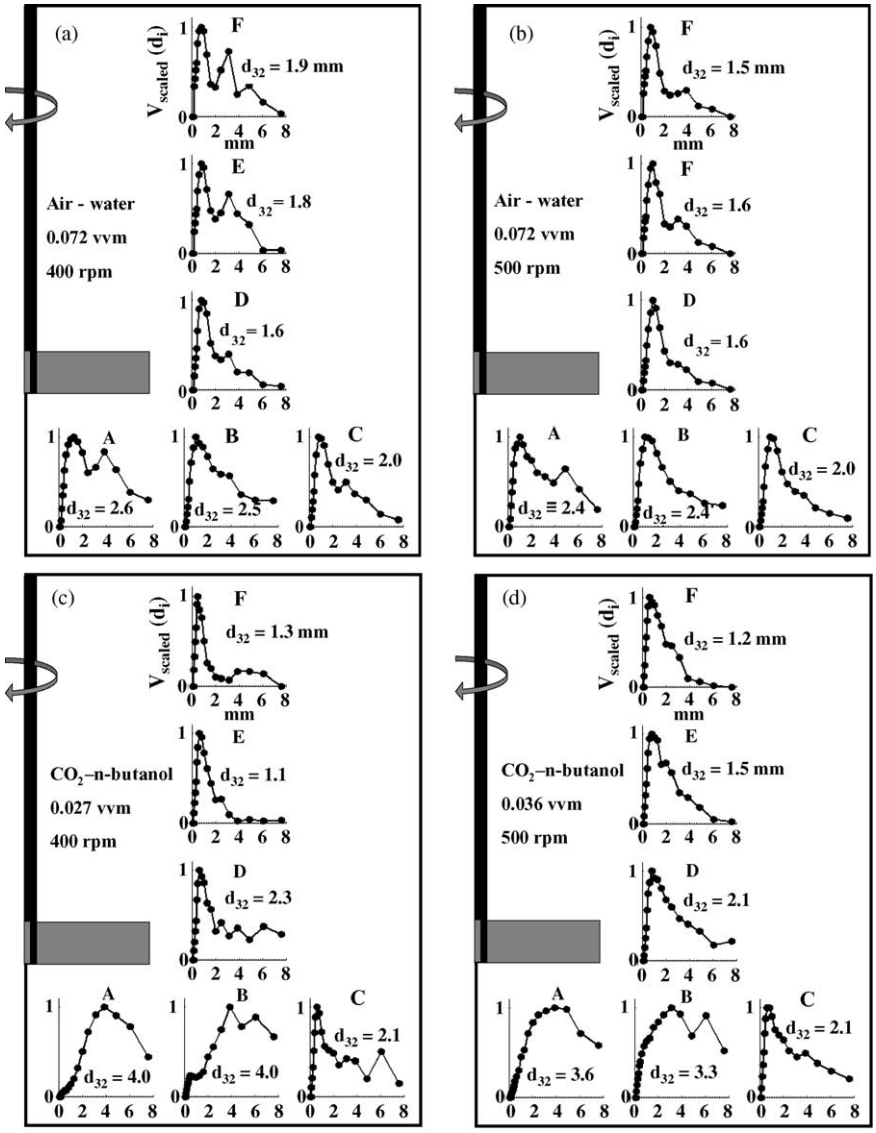

Fig. 6. Local bubble volume densities vs. bubble size (the height of peak scaled to unity) and Sauter mean bubble sizes (d_{32}) in air–water and CO_2–*n*-butanol systems.

and skewed on the left towards small bubble size in both chemical systems. In the air–water system, the BSDs are bimodal throughout the vessel, especially at agitation speed 400 rpm (Fig. 6a). The primary bubbles from the gas distributor could explain the secondary peaks of large bubbles. The measurement of flow fields from air–water system showed that the discharge flow was directed downwards from the impeller towards the bottom of vessel and the flat-blade turbine acted as an axial flow impeller [18]. As a consequence, some primary bubbles bypassed the impeller and recirculated or rose up to the liquid surface without breaking. This was observed also visually and has been observed to occur at low gas flow rates and at high stirring speeds with axial flow impellers [27]. The bimodal BSDs are a result of primary bubbles from the gas distributor and small bubbles from the impeller. The bimodality increases in the air–water system from the tip of impeller towards liquid surface (Fig. 6a). Coalescence of primary bubbles and different rise velocities of small and large bubbles could explain this. The comparison of Fig. 6a and b shows that bubbles become slightly smaller and primary bubbles alter less local BSDs, when stirring speed increases. The larger breakage volume around the impeller seems to explain this.

In contrast to the air–water system, the gas injection had a small effect on local BSDs above the impeller in the CO_2–*n*-butanol system (Fig. 6c and d). The differences in flow fields explain the deviation. In the CO_2–*n*-butanol system, the flow was directed more radially than in the air–water system, from the bottom of vessel to the impeller and onward to the wall of the vessel [18]. As a consequence, most primary bubbles rose directly to the impeller and exposed to the breakage. In the CO_2–*n*-butanol system, bubbles are larger below the impeller

compared to the air–water system, although the smaller surface tension should result into smaller bubble sizes. It appears that only a small amount of CO_2 bubbles enter this region with the liquid flow and the primary bubbles from the gas distributor control the bubble size. In the air–water system, bubbles enter this region not only from the gas distributor but also from the impeller.

The surfactants decrease the tendency of bubble coalescence and the bubble size [3,12,23]. Evidently, tap water and *n*-butanol contained small amounts of surfactants and the exposure of dispersion to the atmosphere caused some contamination as well. For the measurement of liquid flow velocities simultaneously with the BSDs 10 μm tracers were included in both systems [18]. Lindken and Merzkirch [28] investigated the contamination due to tracer particles, but did not observe the settling of particles on the bubble surface. By comparing the experiments with deionized water and water seeded with traces particles they, however, observed a significant drop in the bubble rise velocities especially for bubbles smaller than 3 mm. Yamamoto et al. [29] have estimated that only smaller than 10 μm particles interact with bubbles.

The majority of measured bubbles were close to the minimum detectable bubble size of 0.1 mm. Evidently, bubbles smaller than 0.1 mm existed. The smallest bubbles seem, however, to include a minor fraction of the gas–liquid interfacial area and gas volume and should not contribute significantly the gas–liquid mass transfer. Also, due to long residence times they become easily into gas–liquid equilibrium. The largest detected bubbles were 8.5 mm in both systems thus indicating that bubble coalescence was not inhibited significantly by the presence of surfactants.

The measured bubble sizes agree with the observations of Machon et al. [12], who detected very small bubbles in the deionised water in a baffled 2.65 dm^3 stirred vessel by a photographing technique. The experiments were made at more intense agitation conditions ($Q = \sim 1.0$ vvm, $N = 770$ rpm) than in this work. The results of Machon et al. [12] revealed that 40% of the total number of bubbles was between 40 and 300 μm whereas Sauter mean diameters varied between 2.2 and 3.2 mm. Takahashi et al. [10] measured local BSDs from lean air–deionised water dispersion by a photographing technique and observed mostly smaller than 0.2 mm bubbles. In their experiments Sauter mean diameters varied between 0.35 and 0.7 mm, which are smaller than was observed in this work. Barigou and Greaves [3] investigated local BSDs in a Rushton turbine agitated 1.0 m diameter vessel by using a capillary suction probe. The largest Sauter mean diameters were of the same magnitude as in the present work, although the gassing rates were notably larger.

4.4. Local gas–liquid interfacial areas and gas holdups

Few correlations are available for predicting gas–liquid interfacial area. The correlations derived from the chemical reaction measurements are common but they tend to be specific to the used reaction conditions. The well-known correlation of Calderbank [1] is often used

$$a_t = 1.44 \left[\frac{(P_g/V)^{0.4} \rho_C^{0.2}}{\sigma^{0.6}} \right] \left(\frac{U_s}{U_t} \right)^{0.5}. \quad (18)$$

It is based on the experiments with a light-scattering method. Sridhar and Potter [2] made experiments with the same technique in a 2 dm^3 vessel and verified the Calderbank's correlation at atmospheric pressure and at low gassing rates. They also extended the correlation to higher gassing rates, varying temperatures and pressures. Barigou and Greaves [4] investigated local gas holdups and interfacial areas by a conductivity probe method in a 1.0 m diameter Rushton turbine agitated vessel. Also their results were in good agreement with the correlation of Calderbank [1].

The measured local interfacial areas are compared to the vessel-averaged values obtained from correlation (18) in Fig. 7a and b. The agreement is good, although the variation with the measurement position is large. Interfacial areas are highest below the impeller, especially in positions A and B, which highlights the importance of these regions to the gas–liquid mass transfer. Areas are smallest close to the

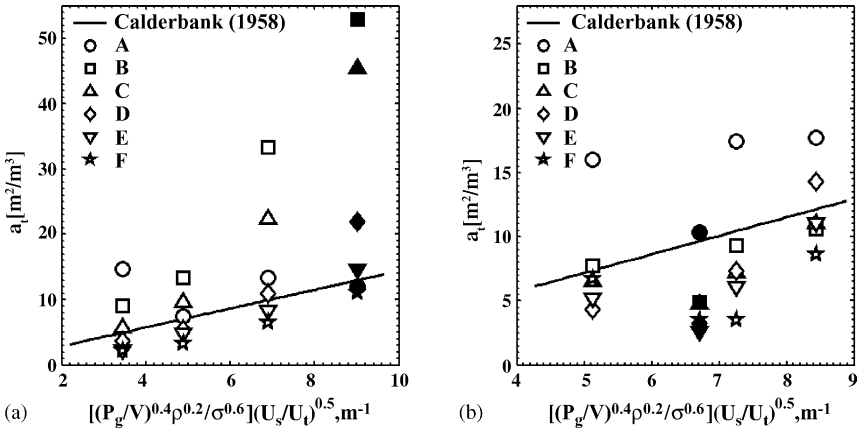

Fig. 7. Measured local (A–F) and predicted [1] gas–liquid interfacial areas: (a) air–water, (b) CO_2–*n*-butanol system, open markers $N = 400$ rpm, filled markers $N = 500$ rpm.

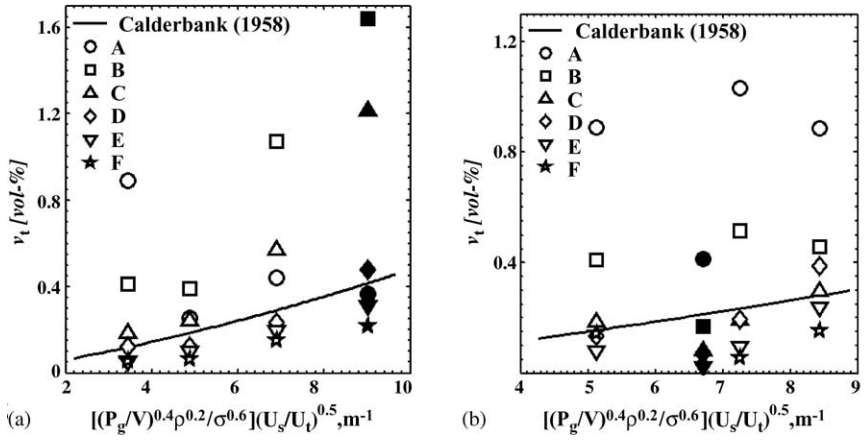

Fig. 8. Measured local (A–F) and predicted [1] gas holdups: (a) air–water, (b) CO_2–*n*-butanol system, open markers $N = 400$ rpm, filled markers $N = 500$ rpm.

liquid surface, but increase with the increasing gassing rate in most experimental positions in both chemical systems. In the air–water system (Fig. 7a) gas–liquid interfacial area increases rapidly with the increasing stirring speed below the impeller in positions A and B. Due to downward flowing liquid there is a balance between the buyoant and drag force and the bubbles become trapped into these regions. Barigou and Greaves [4] have made a similar observation. In the position A, the effect of stirring speed is contrary in the CO_2–*n*-butanol and air–water systems. Apparently, CO_2 bubbles rise from the gas distributor to the impeller at higher velocity decreasing the gas volume fraction below the impeller as the stirring speed increases.

The measured local and the predicted vessel-averaged (Eq. (17)) gas holdups are compared in Fig. 8a and b and show again good agreement. Holdup varies notably with the measurement position, which agrees with the observations of Takahashi and Nienow [11] by a photographing technique in a stirred vessel. Similarly as in the present work Takahashi and Nienow [11] used low gassing rates. The gas holdups varied in their experiments between 0.002 and 0.6 vol.%, which are of the same magnitude as in Fig. 8a and b. Gas holdup is largest in the positions A and B in both systems and at position C at high gassing rate in the air–water system. The comparison of Figs. 7 and 8 shows that the interfacial areas and gas holdups vary similarly in the vessel, which indicates that gas holdup controls the gas–liquid interfacial area.

The experiments at gassing rate 0.036 vvm and stirring speed 400 rpm enabled the comparison of air–water and CO_2–*n*-butanol systems. The comparison is presented in Fig. 9. The measured interfacial areas and holdups are larger in the CO_2–*n*-butanol system, which could be explained by the lower rising velocity of CO_2 bubbles. Assuming that investigated positions A–F represent the inhomogeneities in the vessel, overall interfacial area and holdup can be calculated as an arithmetic average. The averaged gas holdup is for the air–water system 0.2 vol.% and for the CO_2–*n*-butanol system 0.4 vol.%. The corresponding values predicted by correlation (17) are 0.22 and 0.32 vol.% showing close agreement

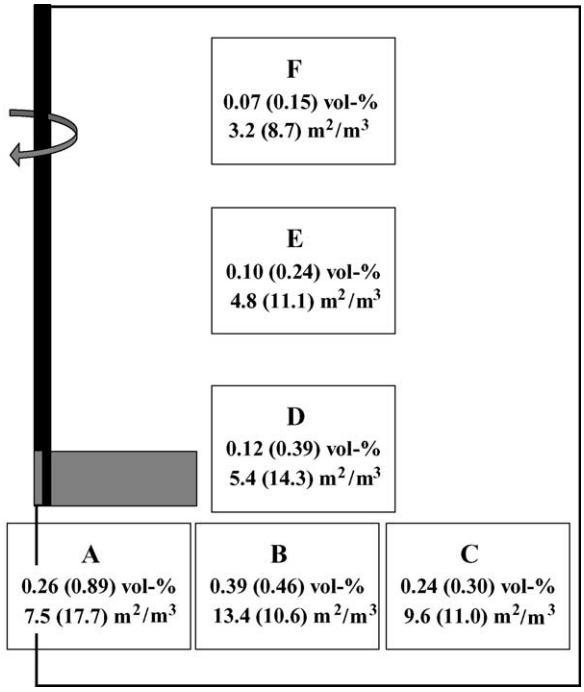

Fig. 9. Measured local gas–liquid interfacial areas and gas holdups from air–water and CO_2–*n*-butanol system (in parentheses), $Q = 0.036$ vvm and $N = 400$ rpm.

against experiments. The averaged interfacial area from the local experiments is for the air–water system 7.3 m^2/m^3 and for the CO_2–*n*-butanol system 12.2 m^2/m^3, which correspond well with the predicted values 7.0 and 12.1 m^2/m^3 from the correlation (18).

5. Conclusions

Local bubble size distributions (BSD), gas–liquid interfacial areas, gas holdups and flow patterns were measured simultaneously from the 14 dm^3 agitated vessel with particle image velocimetry (PIV) technique. Air–water and CO_2–*n*-

butanol systems were investigated. The dispersions were illuminated with the laser light sheet, which minimised the blurriness of images. The calibration experiments with a bubble gel showed that the illumination of dispersion with the light sheet and the identification of bubbles with the thresholding method cause the underestimation of bubble size. In addition, the depth of volume from which a bubble is observed depends on the bubble size. A simple statistical method was developed to correct these bias errors.

The developed correction had a notable effect on the calculated gas–liquid interfacial areas and gas holdups. The flow fields were measured simultaneously and were useful in explaining the variation of BSDs in the vessel. The experiments revealed a significant inhomogeneity of gas–liquid mass transfer conditions in the vessel. The results agree with the well-known vessel-averaged correlations of Calderbank [1]. The present study shows that the flow fields, turbulence quantities, local bubble size distributions, gas–liquid interfacial areas and gas holdups can measured simultaneously with the PIV from an agitated gas–liquid vessel. This is a benefit, since more consistent experimental information is obtained for the validation of simulation tools for agitated gas–liquid reactors.

Acknowledgement

Financial support from Graduate School of Chemical Engineering and KaNeMa project, that is a part of the MANDI program (Multiphase and Industry) coordinated by the National Technology Agency of Finland (TEKES) are acknowledged.

Appendix A. Nomenclature

$a_{b,j}$	bubble surface area (m^2)
a_t	overall gas–liquid area (m^{-1})
$a(d)$	bubble area density (m^{-2})
C_n, C_a, C_v	scaling parameters required to transform bubble number, area and volume density from a size category to another
d	bubble diameter (m)
d_{short}, d_{long}	minor and major axis of identified ellipsoidal bubble (m)
d_{32}	Sauter mean bubble diameter (m)
Δd	width of bubble size category (m)
DOF	depth of field
Δh	auxiliary height parameter in the correction (m)
H_P	height of PIV picture (m)
n_t	bubble concentration (m^{-3})
$n(d)$	bubble number density (m^{-4})
N	agitation speed (rpm)
N_P	number of pictures in an experiment
NB	number of observed bubbles in an experiment
NBC	number of observed bubbles in a bubble size category
NC	number of bubble size categories
$p(d_j,d_i)$	probability to observe a bubble of size category i as a bubble in size category j
P_g	gassed power of mixing (W)
Q	gassing rate of dispersion (m^3 (gas)/m^3 (dispersion)/min)
s	effective depth of field (m)
U_s	superficial gas velocity ($m\,s^{-1}$)
U_t	terminal velocity of bubble ($m\,s^{-1}$).
$v_{b,j}$	bubble volume (m^3)
v_t	gas volume fraction
$v(d)$	gas volume density (m^{-1})
vvm	gas feed rate (m^3 (gas)/m^3 (dispersion)/min)
V	volume of vessel (m^3)
$V(d)$	volume of dispersion from which an individual bubble is observed in an experiment (m^3)
W_P	width of PIV picture (m)

Greek letter

ρ_C	density of continuous phase ($kg\,m^{-3}$)
σ	surface tension ($N\,m^{-1}$)

Subscripts

max	maximum bubble size (m)
min	minimum bubble size (m)
M	measured value
C	corrected value

References

[1] P.H. Calderbank, Physical rate processes in industrial fermentation. Part 1. The interfacial area in gas–liquid contacting with mechanical agitation, Trans. Inst. Chem. Engrs. 36 (1958) 443–463.
[2] T. Sridhar, O.E. Potter, Interfacial areas in gas–liquid stirred vessels, Chem. Eng. Sci. 35 (3) (1980) 683–695.
[3] M. Barigou, M. Greaves, Bubble-size distributions in a mechanically agitated gas–liquid contactor, Chem. Eng. Sci. 47 (8) (1992) 2009–2025.
[4] M. Barigou, M. Greaves, Gas holdup and interfacial area distributions in a mechanically agitated gas–liquid contactor, Chem. Eng. Res. Des. A 74 (1996) 397–405.
[5] V.V. Ranade, Computational Flow Modeling for Chemical Reactor Engineering, Academic Press, San Diego, USA, 2002.
[6] F. Larachi, J. Chaouki, M.P. Dudukovic, Noninvasive and velocimetric monitoring of multiphase flows, Ind. Eng. Chem. Res. 36 (11) (1997) 4476–4503.
[7] P. Mavros, Flow visualization in stirred vessels—a review of experimental techniques, Chem. Eng. Res. Des. A 79 (2001) 113–127.
[8] M. Laakkonen, P. Moilanen, T. Miettinen, K. Saari, M. Honkanen, P. Saarenrinne, J. Aittamaa, Local bubble size distributions in agitated vessel—comparison of three experimental techniques, Chem. Eng. Res. Des. A 83 (2005) 50–58.
[9] J.R. Hernandez-Aguilar, R.G. Coleman, C.O. Gomez, J.A. Finch, A comparison between capillary and imaging techniques for sizing bubbles in flotation systems, Miner. Eng. 17 (2004) 53–61.
[10] K. Takahashi, W.J. McManamey, A. Nienow, Bubble size distributions in impeller region in a gas sparged vessel agitated by a Rushton turbine, J. Chem. Eng. Jpn. 25 (4) (1992) 427–432.

[11] K. Takahashi, A.W. Nienow, Bubble sizes and coalescence rates in an aerated vessel agitated by a Rushton turbine, J. Chem. Eng. Jpn. 26 (5) (1993) 536–542.
[12] V. Machon, A.W. Pacek, A.W. Nienow, Bubble sizes in electrolyte and alcohol solutions in a turbulent stirred vessel, Chem. Eng. Res. Des. 75A (1997) 339–348.
[13] M. Bouaifi, M. Roustan, Bubble size and mass transfer coefficients in dual-impeller agitated reactors, Can. J. Chem. Eng. 76 (3) (1998) 390–397.
[14] G. Hebrard, M. Bouaifi, D. Bastoul, M. Roustan, A comparative study of gas hold-up, bubble size, interfacial area and mass transfer coefficients in stirred gas–liquid reactors and bubble columns, Chem. Eng. Proc. 40 (2) (2001) 97–111.
[15] T.R. Oakley, E. Loth, R.J. Adrian, A two-phase cinematic PIV method for bubbly flows, J. Fluids Eng. 119 (1997) 707–712.
[16] K.T. Kiger, C. Pan, PIV technique for the simultaneous measurement of dlute two-phase flows, J. Fluids Eng. 122 (2002) 811–818.
[17] N.G. Deen, J. Westerweel, E. Delnoij, Two-phase PIV in bubbly flows: status and trends, Chem. Eng. Tech. 25 (1) (2002) 97–101.
[18] M. Honkanen, P. Saarenrinne, Turbulent bubbly flow measurements in a mixing vessel with PIV, in: Proceedings of the 11th International Symposium on Applications of Laser Techniques to Fluid Mechanics, Lisboa, 2002, Paper 3.2.
[19] N. Chigier, Optical imaging of sprays, Prog. Energy Combust. Sci. 17 (3) (1991) 211–262.
[20] M. Honkanen, P. Saarenrinne, Multiphase PIV method with digital object separation methods, in: Proceedings of the Fifth Symposium on Particle Image Velocimetry, Busan, Korea, 2003.
[21] S. Rohani, A. Tadayyon, Determination of particle size distribution by Par-Tec® 100: modeling and experimental results, Part. Part. Syst. Char. 15 (3) (1998) 127–135.
[22] J.O. Hinze, Fundamentals of the hydrodynamic mechanism of splitting in dispersion processes, AIChE J. 1 (3) (1955) 289–295.
[23] G. Marucci, A theory of coalescence, Chem. Eng. Sci. 24 (1969) 975–985.
[24] S.S. Alves, C.I. Maia, J.M.T. Vasconcelos, A.J. Serralheiro, Bubble size in aerated stirred tanks, Chem. Eng. J. 3990 (2002) 1–9.
[25] K. Sano, H. Usui, Interrelations among mixing time, power number and discharge flow rate number in a baffled mixing vessels, J. Chem. Eng. Jpn. 18 (1) (1985) 47–52.
[26] M. Schäfer, P. Wächter, F. Durst, Experimental investigation of local bubble size distributions in stirred vessels using phase Doppler anemometry, in: H.E.A. van den Akker, J.J. Derksen (Eds.), Proceedings of the 10th European Conference on Mixing, 2000, Elsevier, Delft, The Netherlands, pp. 205–212.
[27] A. Bakker, H.E.A. Van Den Akker, Gas–liquid contacting with axial flow impellers, Chem. Eng. Res. Des. A 72 (1994) 573–582.
[28] R. Lindken, W. Merzkirch, A novel PIV technique for measurements in multiphase flows and its application to two-phase bubbly flows, in: Proceedings of the Fourth International Symposium on Particle Image Velocimetry, Göttingen, 2000, p. 1078.
[29] F. Yamamoto, Y. Murai, Ishikawa, Particle tracking velocimetry for dispersions in multiphase flows, in: Proceedings of the Fourth International Symposium on Particle Image Velocimetry, Göttingen, 2000, p. 1064.